Myosin IIA–mediated forces regulate multicellular integrity during vascular sprouting

Christine Yoon[a,†], Colin Choi[a,†], Sarah Stapleton[a,†], Teodelinda Mirabella[a], Caroline Howes[b], Li Dong[b,c], Jessica King[a], Jinling Yang[a], Assad Oberai[b,d], Jeroen Eyckmans[a,e,*], and Christopher S. Chen[a,e,*]

[a]Biological Design Center, Department of Biomedical Engineering, Boston University, Boston, MA 02215;
[b]Department of Mechanical, Aerospace and Nuclear Engineering, Rensselaer Polytechnic Institute, Troy, NY 12180;
[c]The Institute for Computational Engineering and Sciences, University of Texas at Austin, Austin, TX 78712;
[d]Department of Aerospace and Mechanical Engineering, University of Southern California, Los Angeles, CA 90007;
[e]Wyss Institute for Biologically Inspired Engineering, Harvard University, Boston, MA 02115

ABSTRACT **Angiogenic sprouting is a critical process involved in vascular network formation within tissues. During sprouting, tip cells and ensuing stalk cells migrate collectively into the extracellular matrix while preserving cell–cell junctions, forming patent structures that support blood flow. Although several signaling pathways have been identified as controlling sprouting, it remains unclear to what extent this process is mechanoregulated. To address this question, we investigated the role of cellular contractility in sprout morphogenesis, using a biomimetic model of angiogenesis. Three-dimensional maps of mechanical deformations generated by sprouts revealed that mainly leader cells, not stalk cells, exert contractile forces on the surrounding matrix. Surprisingly, inhibiting cellular contractility with blebbistatin did not affect the extent of cellular invasion but resulted in cell–cell dissociation primarily between tip and stalk cells. Closer examination of cell–cell junctions revealed that blebbistatin impaired adherens-junction organization, particularly between tip and stalk cells. Using CRISPR/Cas9-mediated gene editing, we further identified NMIIA as the major isoform responsible for regulating multicellularity and cell contractility during sprouting. Together, these studies reveal a critical role for NMIIA-mediated contractile forces in maintaining multicellularity during sprouting and highlight the central role of forces in regulating cell–cell adhesions during collective motility.**

Monitoring Editor
Valerie Marie Weaver
University of California, San Francisco

Received: Feb 1, 2019
Revised: Jun 13, 2019
Accepted: Jul 1, 2019

INTRODUCTION

Collective migration is a process in which cohorts of cells move in a coordinated manner so that cell–cell contacts are maintained. This is a highly regulated process that is critical in a variety of pathological and developmental morphogenic events such as tumor cell invasion and sprouting angiogenesis (Friedl and Gilmour, 2009; Scarpa and Mayor, 2016). This cooperative movement of cells is of particular importance during sprouting morphogenesis because the endothelial cells that make up new vessels must form patent, nonleaky structures capable of supporting blood flow. The three-dimensional (3D), multicellular structures that form during sprouting are classically composed of leader endothelial cells, or tip cells, that proteolytically degrade the surrounding extracellular matrix to migrate toward sources of angiogenic factors. As they advance, tip cells retain physical cell–cell adhesions with a trailing cohort of stalk cells that form the lumenized trunk of the sprout (Adams and Alitalo, 2007; Carmeliet *et al.*, 2009). Although the molecular drivers of vascular sprouting and tip and stalk cell specification, via the VEGFR2 and Notch1-DLL4 pathways for example, have been extensively described, much less is known about how cellular mechanics and force regulation influence sprout morphogenesis (Gerhardt *et al.*, 2003; Hellström *et al.*, 2007; Benedito *et al.*, 2009).

This article was published online ahead of print in MBoC in Press (http://www.molbiolcell.org/cgi/doi/10.1091/mbc.E19-02-0076) on July 17, 2019.

†These authors contributed equally to this work.

*Address correspondence to: Jeroen Eyckmans (eyckmans@bu.edu); Christopher S. Chen (chencs@bu.edu).

Abbreviations used: AJs, adherens junctions; CRISPR-Cas9, clustered regularly interspaced short palindromic repeats-CRISPR-associated protein 9; NMII, nonmuscle myosin II; NMIIA, nonmuscle myosin II isoform A; NMIIB, nonmuscle myosin II isoform B; ROCK, rho-associated protein kinase; VE-cadherin, vascular endothelial cadherin; VEGF, vascular endothelial growth factor.

The important role of cell-mediated forces in multicellular migration and morphogenesis has been highlighted in various cell types and through a variety of in vitro approaches. For example, in epithelial cells, two-dimensional (2D) assays have been utilized to study the impact of external factors such as substrate stiffness and the role of actomyosin-based contractility in inducing leader cell formation and maintaining coordinated movements of cell cohorts during planar migration (Ng *et al.,* 2012; Rausch *et al.,* 2013). Similarly, in 3D and in vivo assays, studies have demonstrated that cell contractility is needed to enable multicellular 3D invasion and proper morphogenesis of epithelial ductal structures (Ewald *et al.,* 2008; Gjorevski *et al.,* 2015). In endothelial cells, in particular, myosin-mediated cell contractility has been investigated in the context of multicellular organization. For instance, studies using natural and fibrillar matrices have demonstrated that actomyosin-based cell contractility is necessary to support the formation of multicellular networks through processes mimicking vasculogenesis (Lyle *et al.,* 2012; Davidson *et al.,* 2019). In 3D settings, endothelial cells have been shown to depend on actomyosin-based contractile forces to invade their surrounding matrix and maintain sprout structures after invasion (Kniazeva and Putnam, 2009). Intriguingly, several works have begun to quantify the ability of endothelial sprouts to apply contractile forces to their surroundings. For instance, Kniazeva *et al.* (2012) demonstrate that vascular sprout formation is directly correlated with enhanced contractility and the rate at which endothelial cells are able to deform the matrix. Despite this growing body of evidence to suggest the importance of actomyosin-based contractility in sprout morphogenesis, several key questions regarding the spatial organization and magnitude of deformations, as well as a more detailed evaluation of the role of specific myosin isoforms in multicellular sprout structure, still remain.

In this work, we aimed to fill this gap by investigating the role of NMII-mediated cell contractility during angiogenesis, given that many of the signaling pathways driving essential cytoskeletal functions in migrating cells converge on the activation of nonmuscle myosin II (NMII). We first established a general understanding of how endothelial cells within multicellular sprouts generate contractile forces in a microfluidic, biomimetic model of angiogenesis (Nguyen *et al.,* 2013). We then perturbed NMII-generated contractility using a NMII-specific inhibitor, blebbistatin, and CRISPR-Cas9–mediated gene editing to investigate the functional significance of these forces in sprout morphogenesis.

RESULTS

Angiogenic sprouts produce spatially organized matrix deformations

To investigate the importance of cell contractility in sprouting angiogenesis, we first sought to determine if and where forces are generated in multicellular sprout structures in a 3D biomimetic model of angiogenesis previously developed in our lab (Nguyen *et al.,* 2013). Briefly, this microfluidic device consists of two hollow cylindrical channels embedded in a central collagen hydrogel compartment. In one channel, endothelial cells are seeded and form a uniform monolayer, and in the opposing channel, a cocktail of angiogenic factors is supplied to trigger sprouting into the collagen hydrogel. To track the origins of cell-generated forces within sprouts, we adapted this platform so that fiduciary fluorescent beads were embedded into the collagen matrix, enabling measurements of cell-generated matrix deformations (Supplemental Figure S1, A and B). Using methods established for 3D traction force microscopy (TFM; Legant *et al.,* 2010), we measured the magnitude of bead displacements generated by the tip and stalk cells of sprouts that formed 3 to 4 d after the initiation of cocktail exposure and then used these displacements to calculate maps of 3D mechanical deformations in the surrounding ECM. Because collagen matrices exhibit significant nonlinear elastic behavior in response to forces (Münster *et al.,* 2010), one cannot calculate absolute stresses (normalized forces) accurately from these deformations, as would typically be done in 3D TFM protocols. However, the deformation maps nonetheless can be used to define the relative distribution of where cellular forces originate. In these sprouts, we observed significant deformations generated at the leading front of the sprout, particularly by tip cell protrusions (Figure 1A). These displacements are of the same order of magnitude as those generated by other cell types in a similar collagen matrix (Koch *et al.,* 2012; Thievessen *et al.,* 2015). Along the stalk of the sprout, the majority of the measured displacements were minimal in magnitude, suggesting that the tip cell is likely the predominant force-generating unit within a sprout. Closer examination of the displacements revealed that these displacements pointed inward toward the sprout, indicating that forces generated by the tip cell are indeed contractile, as opposed to outward-pushing forces (Figure 1A′).

Inhibition of contractility alters multicellularity of sprout morphogenesis in vitro and in vivo

Given this understanding of the forces generated by angiogenic sprouts, as well as the global importance of actomyosin contractility in producing cellular traction forces, we sought to investigate the morphogenic significance of cell-generated forces during sprouting. To this end, a gradient of angiogenic factors was applied within our in vitro sprouting model in the presence or absence of blebbistatin, a small-molecule inhibitor of NMII that has been shown to reduce cellular traction forces significantly (Bhadriraju *et al.,* 2007; Liu *et al.,* 2010). We exposed the endothelialized channel simultaneously to blebbistatin and angiogenic factors to study how inhibition of NMII may affect various aspects of sprout morphogenesis from the onset. After 5 d of exposure, sprouts were fixed and stained for analysis (Figure 1B). While inhibition of cell contractility had no appreciable effect on the cellular density and speed of invasion from the parent vessel through the collagen matrix (Figure 1, C and D), blebbistatin treatment dramatically increased the frequency of cell–cell breakages in comparison with sprouting achieved in the presence of the vehicle control (Figure 1E).

To parse out whether this breakdown in multicellularity can specifically be attributed to contractility inhibition during sprout elongation, as opposed to other stages of sprout development such as initiation of invasion, we applied varying concentrations of blebbistatin (10, 30, or 50 μM) for 24 h to intact multicellular sprouts that had already extended for 3 d with angiogenic factor stimulation alone. Samples were subsequently fixed, stained for analysis, and evaluated for sprout morphology through high-magnification imaging. While sprouts in the control treatment group formed highly multicellular structures with few sporadic detached cells within the invasion region, treatment with blebbistatin in a dose-dependent manner resulted in an increasing loss of cell–cell contacts between cells (Figure 1F). Given the concentration of force generation in tip cells observed previously, we further categorized the cell–cell breakages as either tip–stalk or stalk–stalk, depending on whether the breakage occurred between a leader cell and its following stalk cell or between two nonleader cells. At the highest concentration of blebbistatin, we saw a significant increase in the number of tip–stalk breakages in comparison with that in the control group. In contrast, this dose of blebbistatin did not induce a significant increase in the incidence of stalk–stalk breakages (Figure 1G). Given the potential

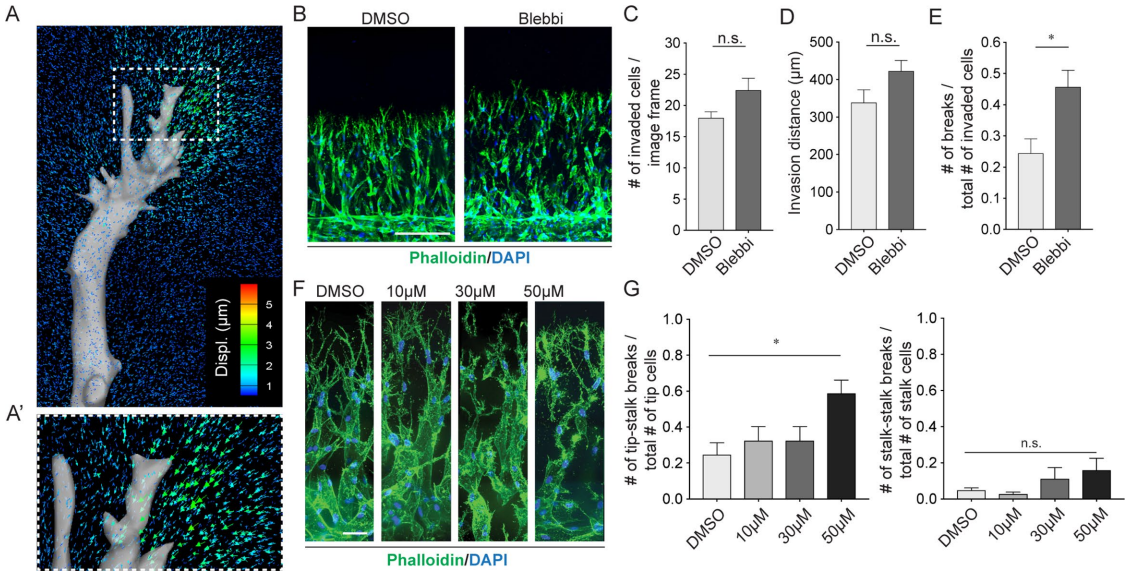

FIGURE 1: Angiogenic sprouts generate contractile forces necessary to maintain multicellular migration. (A) A representative map of matrix deformations (colored arrows) generated by an endothelial sprout (gray). (A') A zoom-in view of the front region of the invading tip cell. (B) Representative F-actin (phalloidin, green) and nuclei (DAPI, blue) images of sprouts at day 5 after sprouting under 30 μM blebbistatin or DMSO control treatment. Scale bar is 200 μm. (C) Quantification of invasion density as measured by the number of invaded nuclei. (D) Quantification of invasion distance as measured by distance from edge of main channel to end of tip cell invasive front. (E) Quantification of cell–cell breakages normalized to total number of invaded cells. (F) Representative F-actin (phalloidin, green) and nuclei (DAPI, blue) images of indicated conditions at day 4 after 24-h blebbistatin treatment. Scale bar is 50 μm. (G) Quantification of detached tip cells (left plot) and stalk cells (right plot) following 24-h blebbistatin treatment. $N_{DMSO} = 3$ devices, 4 fields of view per device, $N_{Blebbi} = 5$ devices, 4 fields of view per device. Bars represent mean ± SEM. * represents $p < 0.05$ as determined by a *t* test (C, D, E) or one-way ANOVA with post hoc Tukey HSD test (G).

off-target effects of a pharmacologic inhibitor such as blebbistatin, we also examined the impact of Y-27632, a selective Rho-associated kinase (ROCK) inhibitor, on sprouting. Indeed, ROCK inhibition led to a similar trend in the loss of tip–stalk contacts during sprout extension (Supplemental Figure S2, A and B).

To establish the relevance of these findings in an in vivo system, we used a mouse retina model in which the vascular network develops across the neuroepithelium during the first week of life. Mouse pups at postnatal day 5 (P5) were injected with blebbistatin and killed 6 h after treatment. Their retinas were subsequently dissected, fixed, and stained for the endothelial cells, using isolectin B4. Corroborating our in vitro findings, a significant number of detached endothelial cells appeared at the migrating front of the developing vascular network (Supplemental Figure S3, A and B). Together, these in vitro and in vivo findings suggest that cytoskeletal forces are not necessarily required for enabling 3D chemotaxis of endothelial cells toward gradients of angiogenic factors, but are required for the maintenance of their multicellularity during sprout extension.

Cell–cell adhesions are disrupted upon contractility inhibition

Vascular endothelial (VE) cadherin is the dominant cadherin involved in adherens junctions (AJs) of ECs and has been shown to regulate vascular permeability, dynamic changes in cell–cell adhesions, and transcellular signaling (Lampugnani *et al.*, 1992; Mehta and Malik, 2006). Cadherins within endothelial AJs have also been shown to link intracellularly with the cytoskeleton by the dynamic, phosphorylation-mediated binding of the intracellular cadherin domain to the actin cytoskeleton via protein complexes consisting of molecular partners such as the catenins (Aberle *et al.*, 1994; Jou *et al.*, 1995). Given the importance of VE cadherin in maintaining cell–cell junctions, as well as the molecular connection between VE cadherin and the actin cytoskeleton, we sought to determine whether alterations in the quality of cell–cell junctions occur in response to NMII inhibition.

To this end, day 3 sprouts were treated with blebbistatin for 24 h and subsequently fixed and immunostained for VE cadherin. High-magnification confocal images of these samples were captured, segmented into regions of tip–stalk and stalk–stalk adhesion, and characterized as either discontinuous or continuous (Figure 2, A and B). Under control conditions, we found that most junctions appeared to have a continuous morphology (Figure 2C), which is characteristic of a more stable phenotype (Bentley *et al.*, 2014). With increasing blebbistatin concentration, tip–stalk adhesions became difficult to observe due to the increase in cell–cell breakages. However, quantification of the tip–stalk adhesions that survived blebbistatin treatment appeared heavily punctate and discontinuous in profile, suggesting that the junctions were unstable (Figure 2C). In fact, under the conditions with the strongest inhibition of contractility, almost all the observed tip–stalk adhesions were classified as discontinuous. Similarly, stalk–stalk cell adhesions shifted to an increasingly unstable adhesion profile in a dose-dependent manner (Figure 2D). At the highest level of blebbistatin treatment, nearly 50% of the stalk–stalk junctions were categorized as discontinuous. Together, these results demonstrate that broad inhibition of contractile activity also causes disorganization of cell–cell junctions, which may in part contribute to the increase in cell–cell breakages observed with blebbistatin treatment.

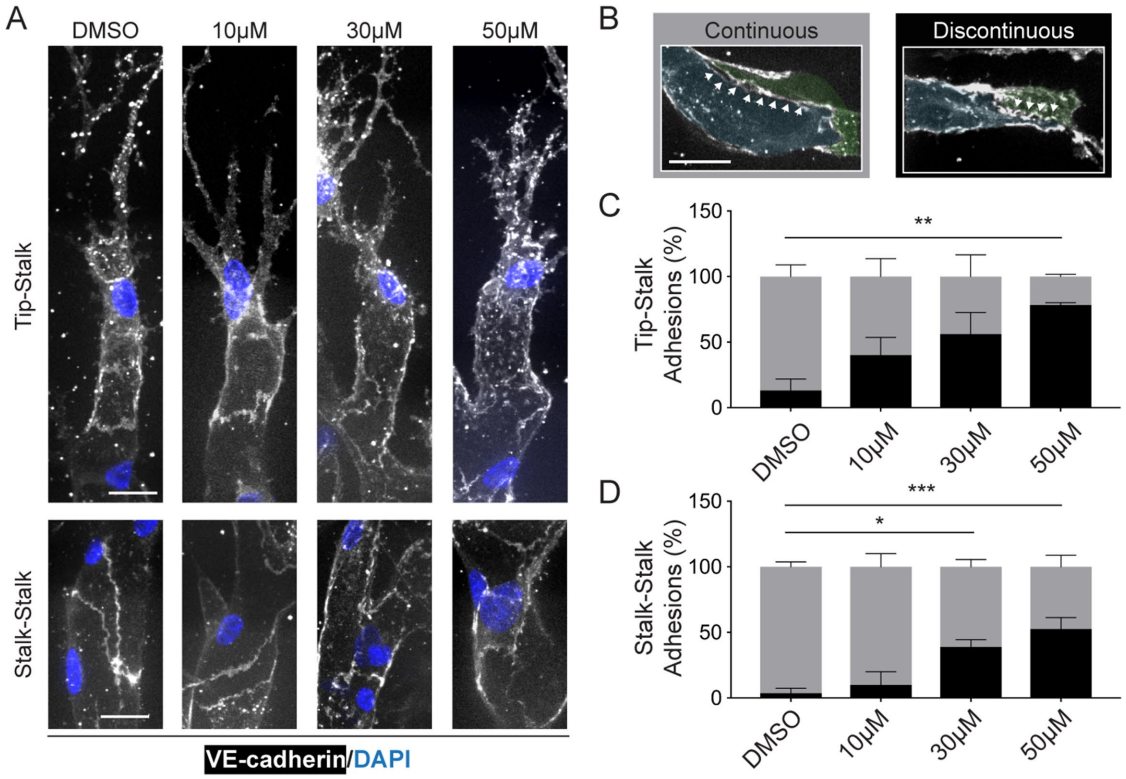

FIGURE 2: Inhibition of myosin-mediated contractility alters the organization of cell–cell adhesions. (A) Representative confocal immunofluorescence images of tip–stalk (top panel) and stalk–stalk (bottom panel) adhesions from indicated conditions at day 4 after 24-h blebbistatin treatment. VE cadherin is shown in white; nuclei are shown in blue. Scale bars are 20 μm. (B) Representative images of catalogued adhesion types. Two neighboring cells are false-colored (blue, green). White arrows show adhesions of interest. Scale bar is 25 μm. (C) Quantification of adhesion profiles of tip–stalk adhesions across treatment groups. (D) Quantification of adhesion profiles of stalk–stalk adhesions across treatment groups. $N = 6$ sprouts per condition from three independent experiments. Bars represent mean ± SEM. * represents $p < 0.05$, ** represents $p < 0.01$, and *** represents $p < 0.001$ as determined by two-way ANOVA with post hoc Dunnett test.

NMIIA is predominantly responsible for maintaining multicellularity during sprouting

The observations connecting cell contractility and cell–cell adhesiveness during sprouting have thus far been based upon pharmacologic inhibition of NMII. However, there is a growing body of evidence highlighting differential roles of distinct nonmuscle myosin II isoforms in various cell types and functions, including regulation of cell–cell junctions (Shih and Yamada, 2010; Jorrisch *et al.*, 2013; Liu *et al.*, 2014; Gutzman *et al.*, 2015). Motivated by these studies and to validate our blebbistatin findings, we sought to investigate the individual contributions of NMII isoforms A and B (henceforth, NMIIA and NMIIB) to mediating the multicellularity of angiogenic sprouting achieved within our system. Using CRISPR-Cas9–mediated gene editing, we generated *MYH9* and *MYH10* knockout endothelial cell lines (hereafter IIA^{KO} and IIB^{KO}, respectively; Figure 3A). While immunofluorescence staining and Western blotting for NMIIA in IIA^{KO} endothelial cells and NMIIB in IIB^{KO} endothelial cells confirmed loss of isoform-specific myosin content, a faint NMIIA signal observed in both immunofluorescence and Western blot analysis suggests a partial (mixed homozygous and heterozygous) knockout (Figure 3, A and B). Nonetheless, IIA^{KO} endothelial cells strikingly appeared to adopt an atypical cell morphology, quantified by the loss of lamellipodia structures (Supplemental Figure S4, A and B), which have been demonstrated to contribute to various endothelial functions including cell migration and the ability to form proper permeability barriers (Breslin *et al.*, 2015; Cao *et al.*, 2017). This morphology resembled that of blebbistatin-treated control cells (Figure 3C). In contrast, IIB^{KO} endothelial cells maintained basic physical features similar to those of the control cells, namely retaining the broad lamellipodia characteristic of normal endothelial cells.

To determine the functional role of each myosin II isoform in sprout morphogenesis, we introduced the IIA^{KO} and IIB^{KO} endothelial cells into our in vitro sprouting model. After 3 d of stimulation with a cocktail of angiogenic factors, the devices were fixed and analyzed for sprout morphology through immunofluorescence staining for CD31 (Figure 3D). Overall, perturbations to NMIIA and NMIIB had no significant effect on the overall ability of cells to invade, as measured by the number of cell nuclei found within the collagen matrix (Figure 3E). Also, whereas loss of NMIIB resulted in no significant changes to sprout length, loss of NMIIA led to a slight but significant reduction in sprout length (Figure 3F). Most importantly, sprouting from IIA^{KO} endothelial cells was characterized by an increase in the portion of cell–cell breakages, whereas loss of NMIIB led to no significant change in this regard (Figure 3G). Taken together, these findings confirm that NMII-mediated contractility is critical for maintaining multicellularity of angiogenic sprouts and highlight the distinct roles of NMIIA and NMIIB in sprouting, with the NMIIA isoform predominantly dictating the morphogenesis of multicellular structures.

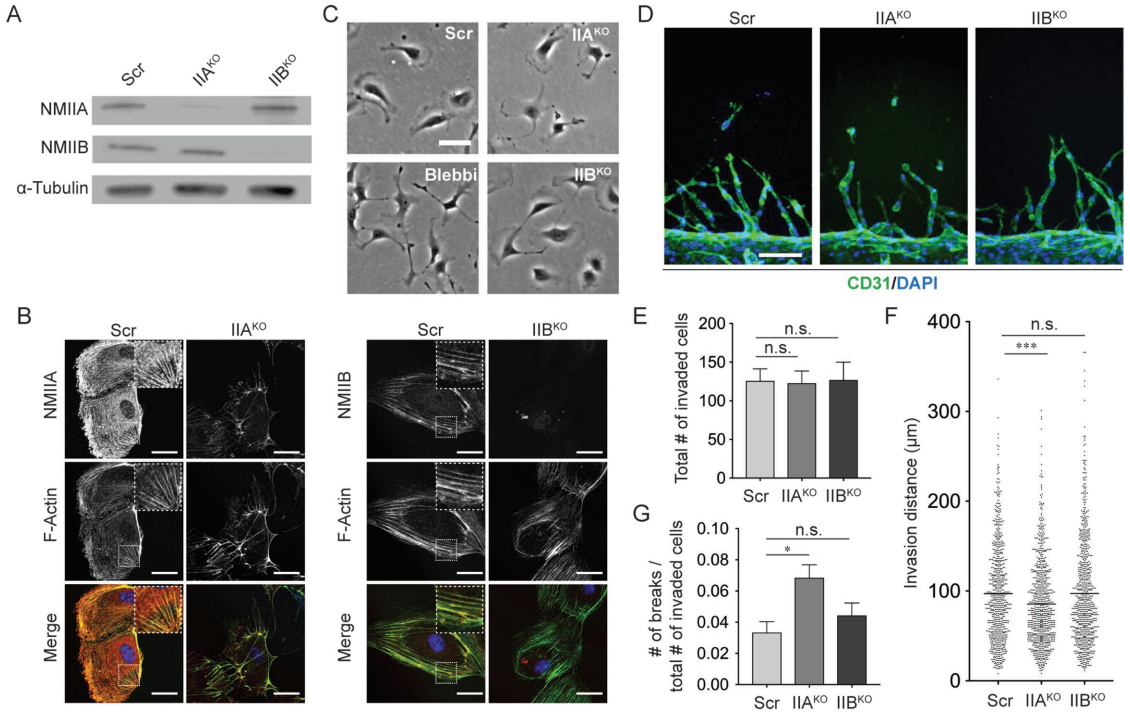

FIGURE 3: Specific loss of the NMII isoform A results in a reduction of sprout multicellularity. (A) Representative Western blots demonstrating diminished protein levels of NMIIA and NMIIB in endothelial cells. (B) Representative immunofluorescence images of endothelial cells stained for NMIIA and NMIIB. Top panels represent NMIIA or NMIIB (white), middle panels represent F-actin (phalloidin, white), and bottom panels are merged images of NMIIA/B (red), F-actin (phalloidin, green), and nuclei (DAPI, blue). Insets show zoomed-in area of corresponding image. Scale bars are 30 μm. (C) Representative bright-field images of endothelial cells cultured in 2D. Scale bar is 50 μm. (D) Representative immunofluorescence images of sprouts stained with CD31 (green) and nuclei (DAPI, blue). Scale bar is 100 μm. (E) Quantification of the number of invaded cells as determined by the number of invaded nuclei. (F) Quantification of invasion distance of sprouts on day 3 after sprouting initiation. Each dot represents one sprout. (G) Quantification of cell–cell breakages normalized by the total number of invaded cells. $N = 715$ sprouts from 16 devices (Scr); 816 sprouts from 17 devices (IIA^{KO}); and 789 sprouts from 17 devices (IIB^{KO}). Bars represent mean ± SEM. ** represents $p < 0.05$ as determined by one-way ANOVA, E and G, or Kruskal–Wallis test, F.

NMIIA is responsible for generating contractile forces in sprouts

Based on these observed differences in the contributions of NMIIA and NMIIB to the multicellular morphogenesis of angiogenic sprouts, we hypothesized that the forces generated by sprouts observed earlier (Figure 1) would largely be dependent on NMIIA. To test this hypothesis, we measured the displacement of fiduciary beads generated by sprouts formed within the in vitro angiogenesis model. Indeed, we found that multicellular sprouts formed by IIA^{KO} endothelial cells produce minimal deformations on the surrounding matrix on the average (Figure 4A). This loss of large bead displacements in the matrix surrounding the leading front of the IIA^{KO} sprouts led to a shift toward smaller deformations in the overall frequency distribution of bead displacements as compared to the Scramble control sprouts (Figure 4, B and C). In line with our previous findings suggesting a more limited role of NMIIB in sprouting, loss of NMIIB did not significantly alter the ability of multicellular sprouts to generate matrix deformations and cellular tractions. This reduction in the ability of NMIIA-deficient sprouts to generate contractile forces, which in turn produce the observed matrix deformations, was also confirmed through 2D traction stress measurements of single cells (Supplemental Figure S5, A and B), demonstrating that NMIIA is the main contractility-generating unit in endothelial cells in both 2D and 3D settings. Overall, these data indicated that generation of cell contractility, through the NMIIA isoform, is essential for maintaining multicellularity during 3D chemotactic migration in the context of sprout morphogenesis.

DISCUSSION

Extensive research investigating the functions of NMII in various cell types and contexts has demonstrated its role as a universal regulator of cell contractility and many cytoskeletal functions. Of particular relevance, myosin has been identified as a key player in regulating migration and cell–cell adhesions. Extensive studies examining the dynamics of cell movements on 2D substrates have demonstrated that loss of myosin activity can lead to reduced migration in most contexts, as detachment of the posterior anchors of migrating cells appears to be hampered without myosin activity (Eddy *et al.*, 2000; Kolega 2003). This migrational slowing has also been confirmed in some studies of cells in 3D contexts (Doyle *et al.*, 2009; Fischer *et al.*, 2009; Petrie *et al.*, 2012). However, this finding is not universal. For example, studies have reported enhanced migration speeds as large stable focal adhesions within cells shift to smaller nascent adhesions (Gupton and Waterman-Storer, 2006; Kim and Wirtz, 2013). Our studies, which demonstrate that blocking cell contractility does not hinder the overall invasiveness of endothelial cells during sprout morphogenesis, build upon this body of evidence suggesting a highly context-dependent role of NMII in cell migration. For instance, in our platform, endothelial invasion is guided by a chemotactic gradient of angiogenic factors, whereas most studies

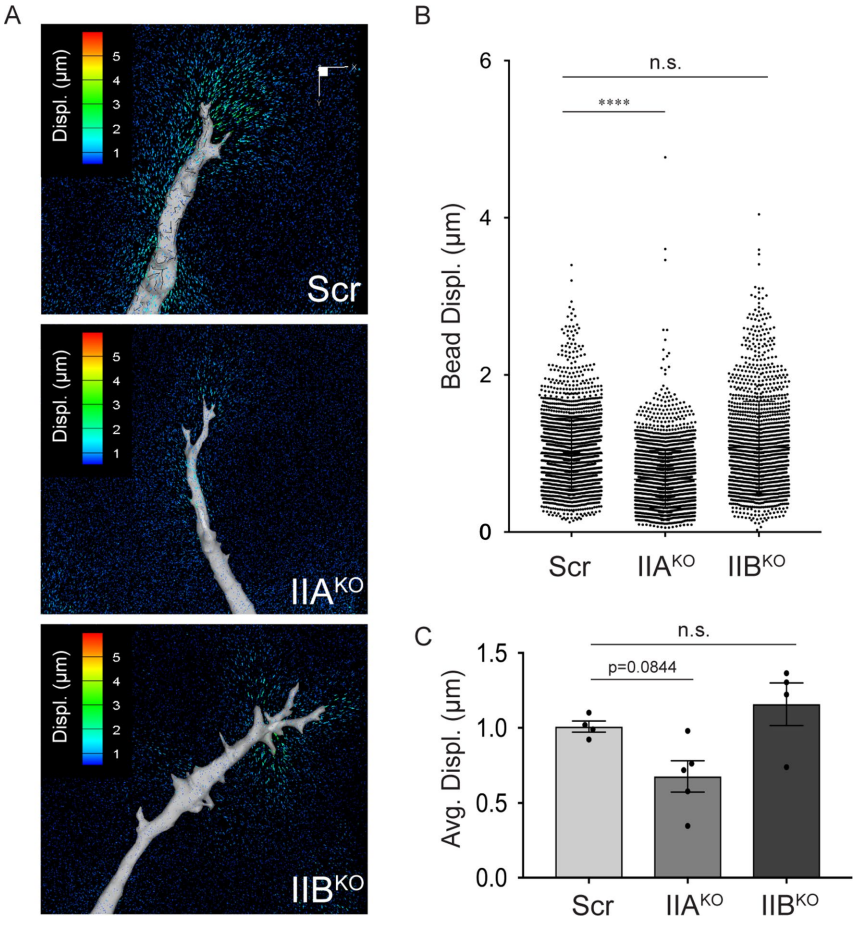

FIGURE 4: NMIIA is the predominant force-generating unit within multicellular sprout structures. (A) Example matrix deformation maps (colored arrows) generated by endothelial sprouts (gray). (B) Each dot represents the magnitude of one displacement vector. The scatterplot is a compilation of $N = 4$ (Scr), 5 (IIAKO), and 4 (IIBKO) sprouts, one sprout per device (= experiment). Only the vectors within 5 μm of the sprout surface were considered for analysis, and displacements over 5 μm are not displayed on the graph. (C) The average bead displacement for each sprout in each condition is displayed. Bars represent mean ± SEM. **** represents $p < 0.0001$ as determined by a Kruskal–Wallis test. Statistical analysis of average displacements was completed via one-way ANOVA with a post hoc Dunnett test.

of myosin inhibition have been in the context of random cell motility. Perhaps in the context of 3D invasion, which is inherently slower than 2D migration because of the requirement for MMP-mediated matrix degradation, migrational persistence is the key determinant of invasion extent. Indeed, myosin has been reported to be required for persistence of a migration axis (Lo *et al.*, 2004; Fischer *et al.*, 2009). In our model system, the presence of a chemotactic gradient may have compensated for the loss of this particular function of NMII. More systematic studies to investigate the role of NMII in chemotaxis-driven invasion of endothelial cells would help to confirm this possibility and improve our basic understanding of the coordinated contribution of NMII, chemotactic gradients, 3D migration, and proteolysis-dependent invasion.

Instead of hindering migration, we observed that reduction in NMII activity led to the fragmentation of multicellular sprouts. This metric of collectiveness, a critically important aspect of neovessel formation, is not often reported in classic in vitro angiogenesis studies but has more recently been incorporated (Shin *et al.*, 2011; Wimmer *et al.*, 2012; Del Amo *et al.*, 2016). Here, we observed that NMII-mediated contractility impacts cell cohesiveness directly and we specifically found that blebbistatin-induced breakages preferentially occur between tip and stalk cells of in vitro angiogenic sprouts. This is likely in part due to the fact that, with blebbistatin treatment, a greater portion of tip–stalk adhesions take on the discontinuous-junction phenotype, which is more prone to disassembly. A similar phenomenon was observed in vivo in the mouse retina model of angiogenesis, where treatment with blebbistatin led to a significant increase in single-cell breakages located at the leading front of the developing vascular plexus. Nonetheless, a more systematic genetic study of NMII loss in the in vivo setting may be needed to validate the role of NMII in vivo fully, given that blebbistatin may target various other cell types that contribute to angiogenesis in vivo (e.g., macrophages and smooth muscle cells).

However, in support of the notion that myosin inhibition selectively induced tip–stalk cell breakages due to the already compromised integrity of their adhesions, a recent study has linked disorganized junction morphologies to adhesions between migratory cells at the migrating front in a scratch wound assay, whereas linear adhesions are observed in less dynamic settings, such as between cells in a quiescent monolayer (Cao *et al.*, 2017). Accordingly, treatment of collectively migrating endothelial cells with VEGF, a well-established disrupter of endothelial adherens junctions, enhances the number of cells that detach from the main cohort (Huveneers *et al.*, 2012; Oubaha *et al.*, 2012). Along the same lines, recent work published by Hayer *et al.* (2016) shows that confluent endothelial monolayers treated with the ROCK inhibitor Y-27632, which has been shown to reduce adherens-junction formation (Abraham *et al.*, 2009), displayed severely diminished coordinated movements. More generally, extensive studies on junctional dynamics, primarily in the context of E-cadherin–mediated adhesions in epithelia, have demonstrated that myosin is critical in mediating junction formation (Shewan *et al.*, 2005; Smutny *et al.*, 2010). Interestingly, recent studies have suggested that also myosin's actin-crosslinking functions, as opposed to its force-generating function per se, are critical to its role in epithelial junction assembly (Ivanov *et al.*, 2006). In the context of endothelial junctions, we have previously found that both force (via myosin) and actin crosslinking (via Rac1) contribute to junction assembly (Liu *et al.*, 2010). Thus, while we were not able to distinguish their roles in this study, it is likely that both contribute to the overall process of junction assembly and stabilization.

Interestingly, in the context of endothelial cell–cell junction assembly dynamics in regulation endothelial barrier function, contractility appears to have a biphasic effect. We and others have previously reported increased cell–cell junction assembly with moderate increases in myosin-mediated contractility in endothelial monolayers (Liu *et al.*, 2010), while others have shown that very high contractility has been shown to abruptly disrupt junctions (Birukova *et al.*, 2004; Valent *et al.*, 2016; Yeh *et al.*, 2018). Bordeleau *et al.* (2017) demonstrated that increasing substrate rigidity, which has been linked to enhanced cell contractility (Califano and Reinhart-King 2010), appears to disrupt EC barrier function. Taken together,

these works investigating the impact of reducing and enhancing cell contractility suggest that there is likely an intermediate level of cell contractility that is needed to maintain the integrity of cell–cell adhesions. Thus, we believe that under physiologic sprouting conditions recapitulated within our in vitro sprouting model, an intermediate level of cell contractility aids in preserving sprout multicellularity, whereas reducing contractility through small-molecule inhibitors or genetic manipulations to NMII leads to cell breakages. Thus, we hypothesize that perturbations to enhance cell contractility under sprouting conditions may result in a similar reduction of sprout multicellularity and should be explored further in future studies.

In addition to identifying a role for myosin in maintaining the multicellularity of invasive sprouts, in this study we also were able to demonstrate that NMII is not used equally in all cells. Using methods from 3D traction force microscopy, we found that sprout morphogenesis occurs with contractile forces mainly exerted by the leader tip cells. This observation is in line with the notion that leader tip cells actively pull on the surrounding matrix while the following stalk cells likely interact more passively with the matrix during sprout elongation (Korff and Augustin, 1999; Du *et al.,* 2016). Pushing forces have been reported in the context of macrophage podosomes and other forms of leukocyte migration (Labernadie *et al.,* 2014), but pulling forces have been the predominant arrangement described in migrating cells (Gardel *et al.,* 2010; Gjorevski *et al.,* 2015). The existence of pulling forces implies that cells proteolytically degrade the ECM to create a path for migration rather than pushing matrix fibers away. Interestingly, stimulation of endothelial cells with VEGF, which primarily activates invasive signaling only in leader tip cells, triggers increased contractile forces and stress fiber formation (Yang *et al.,* 2011; LaValley *et al.,* 2017). The recognition that this NMII activity is focused within the tips of the sprouts gives greater appreciation that the mechanochemical signaling pathway described here—linking force to junction stability—is used selectively, not universally, and underscores the continued need to develop methods for mapping when and where forces are invoked.

Despite the multifaceted approaches employed in these studies to investigate and describe the role of NMII in sprout morphogenesis, several limitations on the various experimental approaches exist. For example, the entirety of the in vitro studies presented in this work were completed using HUVECs as the model cell type. Though HUVECs have been utilized extensively in a broad range of in vitro angiogenesis studies, recent work highlighting differential functions of ECs from specific organs or levels of the vascular hierarchy (Rafii *et al.,* 2016; Hilfenhaus *et al.,* 2018) opens the possibility that the role of NMII in sprout morphogenesis could vary across EC subtypes. Additionally, the in vitro angiogenesis studies carried out in this work have been done utilizing acellular collagen matrices in the absence of supportive cell types such as pericytes and other tissue-specific mural cells; both matrix composition and these ancillary cells have been demonstrated to impact vascular network formation, sprouting, and barrier function (Ribatti *et al.,* 2011; Rao *et al.,* 2012; Kim *et al.,* 2015; Alimperti *et al.,* 2017). Though secondary support cells such as pericytes were excluded from these studies to allow more direct analyses of EC-derived cell forces on sprouting, future studies to investigate the impact of the tissue origin of endothelial cells, the addition of other cell types, and other matrix compositions will be important to assess the universality of the findings reported in this study.

Taken together, our findings and previous work connecting junctional organization with cell dynamics and contractility support the notion that myosin-mediated cell contractility is necessary to maintain physical connectivity of endothelial cells including in the context of multicellular sprout formation.

MATERIALS AND METHODS

Cell culture

Primary human umbilical vein endothelial cells (Lonza) were maintained in endothelial growth medium EGM-2 (Lonza) and used at passages 4–8. Human HEK-293T cells (Clonetech) were cultured in high-glucose DMEM (Hyclone) supplemented with 10% fetal bovine serum (Hyclone), 100 U ml^{-1} penicillin, 100 µg ml^{-1} streptomycin (Life Technologies) and 2 mM L-glutamine (Life Technologies). All cell types were maintained at 37°C in 5% CO_2 in a humidified incubator.

Antibodies and reagents

The following antibodies and reagents were utilized for the immunofluorescence and Western blot analyses presented: mouse anti-VE-cadherin antibody (1:100; sc-9989; Santa Cruz), mouse anti-CD31 antibody (1:200; JC70A; Dako), donkey anti-mouse secondary (1:500; Alexa Fluor 568 A10037; Invitrogen), goat anti-mouse secondary (1:500; Alexa Fluor 568 A11031; Invitrogen), Alexa Fluor 488-conjugated phalloidin (1:500; A12379; Invitrogen), rat anti-mouse VE-Cadherin antibody (1:50; clone 11D4.1; BD Bioscience), donkey anti-rat secondary (1:300; Cy3; Jackson Lab), anti-rat IgG Alexa Fluor 568 (1:300; Invitrogen), isolectin B4 (Vectorlabs), rabbit anti-nonmuscle myosin heavy chain II-A (1:10,000; 909802l; BioLegend), rabbit anti-Non-muscle myosin heavy chain II-B (1:10,000; ABT1340; Millipore), goat anti-rabbit secondary (1:500, Alexa Fluor 568 A11011; Invitrogen), and DAPI (Sigma).

Lentiviral-mediated CRISPR genome editing

Stable CRISPR-knockout HUVEC cell lines were generated using guide (g)RNAs formulated by the Optimized CRISPR Design Tool (F. Zhang). The following gRNA sequences were designed and utilized: TCAAGGAGCGTTACTACTCA Exon 1 for MYH9 and TGGATTCCATCAGAACGCCATGG Exon 1 for MYH10. Individual gRNA-containing plentiCRISPRv2 plasmids were cotransfected with pVSVG, pRSV-REV, and pMDLg/pRRE packaging plasmids into HEK-293T cells using calcium phosphate transfection. After 48 h, viral supernatants were collected, concentrated using PEG-IT viral precipitator (SBI), and resuspended in phosphate-buffered saline (PBS). HUVECs were transduced in growth medium overnight, and medium was replaced the following morning. At 48 h after infection, cells were replated and selected with 2 µg ml^{-1} puromycin for 3–4 d. All CRISPR modifications were verified by standard Western blot techniques and immunofluorescence staining.

Microfluidic device fabrication and seeding for blebbistatin experiments

For blebbistatin treatment experiments, microfluidic devices were fabricated using soft lithography techniques as previously described (Nguyen *et al.,* 2013). Briefly, the polydimethylsiloxane (PDMS) device consists of a central region in which a collagen prepolymer solution is cast around two cylindrical acupuncture needles. Upon hydrogel formation, the acupuncture needles are removed from the device to generate two hollow cylindrical channels fully embedded within the collagen. Each of the channels is connected to two reservoirs that serve as ports for cell seeding and media replenishment. For device seeding, cells were trypsinized, reconstituted at 10^6 cells ml^{-1}, and seeded into one of the two hollow channels. The devices were inverted to allow cells to adhere to the top surface of the channel for 3 min, and then flipped

upright to allow cells to adhere to the bottom surface of the channel for 3 min. Unattached cells in the channel were then thoroughly flushed out with PBS. EGM-2 was added immediately thereafter and the devices were placed on a platform rocker (BenchRocker, BR2000) in a humidified incubator. Cells were cultured in channels for 1 d before the angiogenic factors MCP-1, VEGF, PMA, and S1P (MVPS cocktail), defined in Nguyen *et al.* (2013), were introduced.

Blebbistatin treatment of in vitro sprouts in device

For 5-d blebbistatin treatment, cells were treated simultaneously with 30 µM blebbistatin (Tocris) and an MVPS gradient. Blebbistatin treatment was applied to both the cell channel and the MVPS source channel so that no gradient of inhibitor was established. Blebbistatin-containing cocktail and cell media were refreshed daily. For 24-h blebbistatin treatment of extending sprouts, cells were cultured in the device under an MVPS gradient for 3 d before blebbistatin treatment. During this period, medium in the cell channel and cocktail in the source channel were refreshed daily. Following 3 d of sprouting, blebbistatin or vehicle control was added to cell medium and MVPS cocktail and used to refresh the device. Blebbistatin concentrations in the device were 10, 30, and 50 µM, and vehicle control was DMSO (added int amount used for 50 µM blebbistatin treatment). Y-27632 (25 µM, Tocris) experiments were performed in the same manner. At the end of all sprouting experiments, devices were fixed in warm 3% paraformaldehyde for 25 min at 37°C and subsequently rinsed three times with PBS before permeabilization with 0.1% Triton-X for 20 min. For VE-cadherin staining, devices were blocked with 3% BSA in PBS overnight, then treated with primary VE-cadherin antibody (1:100) in 3% BSA in PBS overnight, rinsed for 6 h, and incubated with Alexa Fluor-conjugated secondary antibody (1:500), Alexa Fluor-conjugated phalloidin (1:100), and DAPI (1:500, Sigma).

Image acquisition and processing

All brightfield images of sprouts were acquired with a Nikon TE200 epifluorescence microscope (Nikon Instruments) using a 10× objective. All confocal microscopy for immunofluorescence samples was completed with a Yokogawa CSU-21/Zeiss Axiovert 200M inverted spinning disk microscope equipped with an Evolve EMCCD camera (Photometrics). ImageJ (NIH) was used to merge channels, perform Z-projection for all confocal stacks, and generate longitudinal and transverse cross-sections. Custom MATLAB scripts and ImageJ were used to stitch images together.

Quantification of blebbistatin-induced cell–cell breakages

For each device, 40× confocal 3D image stacks were collected at three locations equidistant from each other along the channel. Image collections were centered on the midpoint of the channel in the *z*, or vertical, direction. Individual image stacks contained 100 slices, taken at 2-µm increments in the *z* direction. Quantification was completed in a blinded manner by scrolling through each 200-µm depth set after images were stitched together to capture full invasion length. Numerical data were collected on 1) number of tip cells, 2) number of detached tip cells, 3) number of stalk cells, and 4) number of detached stalk cells. Tip cells were defined morphologically as cells in the leading half of the cellular invasion distance (defined from the front of leading cells back to the near edge of the main cell channel) and the presence of multiple, long actin-rich protrusions directed toward the gradient source. All other cells were assigned as stalk cells, which were generally located in the back half of the invasion and lacked actin-rich protrusions.

Mouse retina studies

Mice were housed in accordance with the Institutional Animal Care and Use Committee at Boston University and the National Institutes of Health guidelines. C57Black/6 mice from Taconic were used for breeding purposes. Pups at postnatal day 5 (P5) were injected intraperitoneally with either 5 µl of vehicle (DMSO) or blebbistatin (50 mM), diluted in OptiMEM for a total of 50 µl in injection volume. At 6 h after injection, pups were killed and retinas dissected after fixation in 4% paraformaldehyde. Fixed retinas were then processed for 1 h in 3% BSA and 0.5% Triton X-100. Retinas were whole-mounted, and images were acquired with 40× 1.1 N.A. water-immersion objective.

Microfluidic device fabrication and seeding for NMII CRISPR experiments

Polydimethylsiloxane (PDMS, Sylgard 184, Dow-Corning) was mixed at a ratio of 10:1 (base:curing agent) and cured overnight at 60°C around stereolithography-printed molds (ProtoLabs) designed to maintain key features and dimensions of the microfluidic device from Nguyen *et al.* (2013). This alternative method of device fabrication was employed solely to improve throughput of device manufacture. The PDMS was cut from the master mold, trimmed, surface-activated by plasma treatment for 30 s, and bonded to glass coverslips. PDMS devices were surface-functionalized using (3-glycidyloxypropyl)trimethoxysilane (Sigma) for 3 h and maintained in an empty vacuum chamber overnight as an alternative method to the one described in Nguyen *et al.* (2013). All other collagen formation and cell seeding steps were similar to that of the blebbistatin experiments detailed above. For devices used in bead displacement studies, two types of carboxylated polystyrene beads (0.19 µm Dragon Green, 1:250, and 0.22 µm Flash Red, 1:400, Bangs Labs) were added to the collagen solution immediately before polymerization. Cells were cultured in channels for 1 d before angiogenic factors were introduced.

In these studies, an alternative cocktail of factors was employed: hepatocyte growth factor (5.5 ng ml^{-1}, R&D Systems), vascular endothelial growth factor (3 ng ml^{-1}, R&D Systems), phorbol myristate acetate (25 ng ml^{-1}, R&D Systems), and sphingosine-1-phosphate (2 nM, Cayman Chemical). This cocktail of factors was optimized to achieve low sprouting density in this sprouting platform so that bead displacement measurements from singular sprouts could be measured. For consistency, this cocktail was also used for morphogenesis studies using the NMII CRISPR cells.

For these studies, devices were fixed 3 d after the addition of the angiogenic cocktail with 4% paraformaldehyde in endothelial basal media (EBM) at room temperature for 30 min. Devices were rinsed three times with PBS and permeabilized with 0.2% Triton X-100 in PBS for 15 min. Devices were blocked overnight with 2% BSA in PBS, incubated with mouse anti-human CD31 antibody (1:200, Dako) in PBS overnight, rinsed in PBS, and stained with Alexa Fluor-conjugated secondary antibody (1:500) and DAPI (1:500).

Quantification of sprout length and cell–cell breakages of $NMII^{KO}$ sprouts

For each device, confocal Z-stack images of the entire cell channel were acquired with a 10× air objective. These fluorescence images were adjusted for brightness and contrast using ImageJ. Total cells invaded out of the main endothelial channel were quantified by counting the number of nuclei within the matrix and completed in a blinded manner. Sprout length was measured by quantifying the perpendicular distance from the leading tip of an intact sprout to the base of that sprout. Quantification of the number of cell–cell

breakages was completed in a blinded manner by manually scrolling through grayscale Z-stack micrographs of sprouts immunostained for CD31. CD31 immunostaining was utilized for this analysis in order to visualize endothelial cell membranes and regions of cell–cell contacts most robustly, allowing global measures of spout multicellularity at low magnification.

Three-dimensional collagen bead displacement measurements and quantification

Sprouts formed between day 3 and day 4 after exposure to cocktail were analyzed for these experiments. Before imaging, cells were labeled with Deep Red Cell Mask (1:2000, Invitrogen) for 8 min and the device was set on the confocal microscope stage equipped with an environmental chamber to maintain 37°C temperature and 5% CO_2 levels. Devices were allowed to equilibrate on the stage for 10–20 min before imaging. Intact, multicellular sprouts that were sufficiently isolated from surrounding cells were identified, and "stressed"-state Z-stack images of the sprout and beads were captured with a 0.8-μm step size. Immediately afterward, devices were treated with 0.1% Triton-X in PBS for 30 min to allow cell lysis and relaxation of the matrix. Finally, "zero-stress" images of the same region of interest were captured. Bead displacement maps were generated as previously described in Legant *et al.* (2010). Briefly, sprout surface meshes were generated through manual border identification in Amira (Visage Imaging). The 2D surface mesh of the sprout was generated from the segmented image and imported into Hypermesh (Altair) as a stereolithography file. The final surface meshes were imported into Abaqus (Dassault Systèmes) for finite element analysis. Bead displacements were calculated through a custom MATLAB code. Renderings of bead displacements and the corresponding sprout surface meshes were generated using Tecplot 360 (Tecplot).

2D dextran gel fabrication

Arginine-glycine-aspartate (RGD)-modified dextran hydrogels were employed to measure 2D traction stresses generated by NMIIKO cells. The dextran gel was prepared as previously described in Trappmann *et al.* (2017), mixed with fluorescent fiduciary beads (0.19 μm Dragon Green, 1:400, Bangs Labs), and cast between a glass-bottomed 35-mm dish (MatTek) and a SurfaSil (Sigma)-treated glass coverslip. After gel polymerization at room temperature for 45 min, PBS was added to the gel and the top coverslip was removed with tweezers. The gel was washed twice with PBS and seeded with endothelial cells at 30,000 cells/substrate for 1 h. Afterward, any remaining unattached cells were washed with EGM-2 and substrates were returned to the incubator overnight.

Two-dimensional bead displacement imaging and traction force microscopy analysis

Prior to TFM measurements, cells were labeled with a membrane dye (Deep Red Cell Mask, Invitrogen) diluted in growth medium (1:4000) for 3 min before being washed once and left to equilibrate under normal growth conditions for at least 1 h.

Traction forces exerted by cells were computed by imaging the fiduciary fluorescent beads embedded in the dextran gel and measuring their displacement using previously described methods (Tseng *et al.*, 2012; software available at https://sites.google.com/site/qingzongtseng/tfm). Briefly, images of surface-level beads within and around the patterned multicellular square islands were captured at least 20 min after transfer of substrates to the microscope (Yokogawa CSU-21/Zeiss Axiovert 200M inverted spinning disk microscope with a Zeiss LD C-Apochromat 25×, 0.8 N.A. objective and an Evolve EMCCD camera) environmental chamber (37°C, 5% CO_2). Once all "stressed" images were obtained, "relaxed" images illustrating the zero-stress state locations of the beads were obtained by lysing cells with 0.1% vol/vol Triton-X and allowing the substrate to equilibrate for at least 60 s.

Bead displacement vectors were determined using the particle image velocimetry ImageJ plug-in (Tseng *et al.*, 2012) with a final window size of ~18.2 × 18.2 μm. Based on these bead displacement vectors, traction stress fields were generated using the Fourier transform traction cytometry ImageJ plug-in (Tseng *et al.*, 2012). A regularization parameter of 4.0×10^{-9} was set for all traction stress reconstructions, and a Young's modulus of 2500 Pa was used based on atomic force microscopy characterization from Trappmann *et al.* (2017). The root-mean-square (RMS) traction stresses were calculated from the vectors that were greater in magnitude than that of background vectors, defined manually for each analyzed cell.

ACKNOWLEDGMENTS

We are grateful to Megan Griebel and Jerry Shih for technical assistance. This work was supported by grants from the National Institutes of Health (EB00262, HL115553), the NSF Science and Technology Center for Engineering Mechanobiology (CMMI-1548571), and the Boston University Biological Design Center.

REFERENCES

Aberle H, Butz S, Stappert J, Weissig H, Kemler R, Hoschuetzky H (1994). Assembly of the cadherin–catenin complex in vitro with recombinant proteins. J Cell Sci 9, 3655–3663.

Abraham S, Yeo M, Montero-Balaguer M, Paterson H, Dejana E, Marshall CJ, Mavria G (2009). VE-cadherin-mediated cell–cell interaction suppresses sprouting via signaling to MLC2 phosphorylation. Curr Biol 19, 668–674.

Adams RH, Alitalo K (2007). Molecular regulation of angiogenesis and lymphangiogenesis. Nat Rev Mol Cell Biol 8, 464–478.

Alimperti S, Mirabella T, Bajaj V, Polacheck W, Pirone DM, Duffield J, Eyckmans J, Assoian, RK, Chen CS (2017). Three-dimensional biomimetic vascular model reveals a RhoA, Rac1, and N-cadherin balance in mural cell–endothelial cell-regulated barrier function. Proc Natl Acad Sci USA 114, 8758–8763.

Benedito R, Roca C, Sörensen I, Adams S, Gossler A, Fruttiger M, Adams RH (2009). The notch ligands Dll4 and Jagged1 have opposing effects on angiogenesis. Cell 137, 1124–1135.

Bentley K, Franco CA, Philippides A, Blanco R, Dierkes M, Gebala V, Stanchi F, Jones M, Aspalter IM, Cagna G, *et al.* (2014). The role of differential VE-cadherin dynamics in cell rearrangement during angiogenesis. Nat Cell Biol 16, 309–321.

Bhadriraju K, Yang M, Alom Ruiz S, Pirone D, Tan J, Chen CS (2007). Activation of ROCK by RhoA is regulated by cell adhesion, shape, and cytoskeletal tension. Exp Cell Res 313, 3616–3623.

Birukova AA, Smurova K, Birukov KG, Kaibuchi K, Garcia JG, Verin AD (2004). Role of Rho GTPases in thrombin-induced lung vascular endothelial cells barrier dysfunction. Microvasc Res 67, 64–77.

Bordeleau F, Mason BN, Lollis EM, Mazzola M, Zanotelli MR, Somasegar S, Califano JP, Montague C, LaValley DJ, Huynh J, *et al.* (2017). Matrix stiffening promotes a tumor vasculature phenotype. Proc Natl Acad Sci USA 114, 492–497.

Breslin JW, Zhang XE, Worthylake RA, Souza-Smith FM (2015) Involvement of local lamellipodia in endothelial barrier function. PLoS One 10, e0117970.

Califano JP, Reinhart-King CA (2010). Substrate stiffness and cell area predict cellular traction stresses in single cells and cells in contact. Cell Mol Bioeng 3, 68–75.

Cao J, Ehling M, März S, Seebach J, Tarbashevich K, Sixta T, Pitulescu ME, Werner AC, Flach B, Montanez E, *et al.* (2017). Polarized actin and VE-cadherin dynamics regulate junctional remodelling and cell migration during sprouting angiogenesis. Nat Commun 8, 2210.

Carmeliet P, De Smet F, Loges S, Mazzone M (2009). Branching morphogenesis and antiangiogenesis candidates: tip cells lead the way. Nat Rev Clin Oncol 6, 315–326.

Davidson CD, Wang WY, Zaimi I, Jayco DKP, Baker BM (2019). Cell force-mediated matrix reorganization underlies multicellular network assembly. Sci Rep 9, 12.

Del Amo C, Borau C, Gutiérrez R, Asín J, García-Aznar JM (2016). Quantification of angiogenic sprouting under different growth factors in a microfluidic platform. J Biomech 49, 1340–1346.
Doyle AD, Wang FW, Matsumoto K, Yamada KM (2009). One-dimensional topography underlies three-dimensional fibrillar cell migration. J Cel Biol 184, 481–490.
Du Y, Herath SCB, Wang Q, Wang D, Asada HH, Chen PCY (2016). Three-dimensional characterization of mechanical interactions between endothelial cells and extracellular matrix during angiogenic sprouting. Sci Rep 6, 21362.
Eddy RJ, Pierini LM, Matsumura F, Maxfield FR (2000). Ca2+-dependent myosin II activation is required for uropod retraction during neutrophil migration. J Cell Sci 113, 1287–1298.
Ewald AJ, Brenot A, Duong M, Chan BS, Werb Z (2008). Collective epithelial migration and cell rearrangements drive mammary branching morphogenesis. Dev Cell 14, 570–581.
Fischer RS, Gardel M, Ma X, Adelstein RS, Waterman CM (2009). Local cortical tension by myosin II guides 3D endothelial cell branching. Curr Biol 19, 260–265.
Friedl P, Gilmour D (2009). Collective cell migration in morphogenesis, regeneration and cancer. Nat Rev Mol Cell Biol 10, 445–457.
Gardel ML, Schneider IC, Aratyn-Schaus Y, Waterman CM (2010). Mechanical integration of actin and adhesion dynamics in cell migration. Annu Rev Cell Dev Biol 26, 315–333.
Gerhardt H, Golding M, Fruttiger M, Ruhrberg C, Lundkvist A, Abramsson A, Jeltsch M, Mitchell C, Alitalo K, Shima D, *et al*. (2003). VEGF guides angiogenic sprouting utilizing endothelial tip cell filopodia. J Cell Biol 161, 1163–1177.
Gjorevski N, Piotrowski AS, Varner VD, Nelson CM (2015). Dynamic tensile forces drive collective cell migration through three-dimensional extracellular matrices. Sci Rep 5, 11458.
Gupton SL, Waterman-Storer CM (2006). Spatiotemporal feedback between actomyosin and focal-adhesion systems optimizes rapid cell migration. Cell 125, 1361–1374.
Gutzman JH, Sahu SU, Kwas C (2015). Non-muscle myosin IIA and IIB differentially regulate cell shape changes during zebrafish brain morphogenesis. Dev Biol 397, 103–115.
Hayer A, Shao L, Chung M, Joubert LM, Yang HW, Tsai FC, Bisaria A, Betzig E, Meyer T (2016). Engulfed cadherin fingers are polarized junctional structures between collectively migrating endothelial cells. Nat Cell Biol 18, 1311–1323.
Hellström M, Phng LK, Hofmann JJ, Wallgard E, Coultas L, Lindblom P, Alva J, Nilsson AK, Karlsson L, Gaiano N, *et al*. (2007). Dll4 signaling through Notch1 regulates formation of tip cells during angiogenesis. Nature 445, 776–780.
Hilfenhaus G, Nguyen DP, Freshman J, Prajapati D, Ma F, Song D, Ziyad S, Cuadrado M, Pellegrini M, Bustelo XR, Iruela-Arispe ML (2018). Vav3-induced cytoskeletal dynamics contribute to heterotypic properties of endothelial barriers. J Cell Biol 217, 2813–2830.
Huveneers S, Oldenburg J, Spanjaard E, van der Krogt G, Grigoriev I, Akhmanova A, Rehmann H, de Rooij J (2012). Vinculin associates with endothelial VE-cadherin junctions to control force-dependent remodeling. J Cell Biol 196, 641–652.
Ivanov AI, McCall IC, Babbin B, Samarin SN, Nusrat A, Parkos CA (2006). Microtubules regulate disassembly of epithelial apical junctions. BMC Cell Biol 7, 12.
Jorrisch MH, Shih W, Yamada S (2013). Myosin IIA deficient cells migrate efficiently despite reduced traction forces at cell periphery. Biol Open 2, 368–372.
Jou TS, Stewart DB, Stappert J, Nelson WJ, Marrs JA (1995). Genetic and biochemical dissection of protein linkages in the cadherin–catenin complex. Proc Natl Acad Sci USA 92, 5067–5071.
Kim DH, Wirtz D (2013). Focal adhesion size uniquely predicts cell migration. FASEB J 27, 1351–1361.
Kim J, Chung M, Kim S, Jo DH, Kim JH, Jeon NL (2015). Engineering of a biomimetic pericyte-covered 3D microvascular network. PLoS One 10, e0133880.
Kniazeva E, Putman AJ (2009). Endothelial cell traction and ECM density influence both capillary morphogenesis and maintenance in 3-D. Am J Physiol Cell Physiol 297, 179–187.
Kniazeva E, Weidling JW, Singh R, Botvinick EL, Digman MA, Gratton E, Putman AJ (2012). Quantification of local matrix deformations and mechanical properties during capillary morphogenesis in 3D. Integr Biol 4, 431–439.
Koch TM, Münster S, Bonakdar N, Butler JP, Fabry B (2012). 3D traction forces in cancer cell invasion. PLoS One 7, e33476.
Kolega, J (2003). Asymmetric distribution of myosin IIB in migrating endothelial cells is regulated by a rho-dependent kinase and contributes to tail retraction. Mol Biol Cell 14, 4745–4757.
Korff T, Augustin HG (1999). Tensional forces in fibrillar extracellular matrices control directional capillary sprouting. J Cell Sci 112, 3249–3258.
Labernadie A, Bouissou A, Delobelle P, Balor S, Voituriez R, Proag A, Fourquaux I, Thibault C, Vieu C, Poincloux R, *et al*. (2014). Protrusion force microscopy reveals oscillatory force generation and mechanosensing activity of human macrophage podosomes. Nat Commun 5, 5343.
Lampugnani MG, Resnati M, Raiteri M, Pigott R, Pisacane A, Houen G, Ruco LP, Dejana E (1992). A novel endothelial-specific membrane protein is a marker of cell–cell contacts. J Cell Biol 118, 1511–1522.
LaValley DJ, Zanotelli MR, Bordeleau F, Wang W, Schwager SC, Reinhart-King CA (2017). Matrix stiffness enhances VEGFR-2 internalization, signaling, and proliferation in endothelial cells. Converg Sci Phys Oncol 3, 044001.
Legant WR, Miller JS, Blakely BL, Cohen DM, Genin GM, Chen CS (2010). Measurement of mechanical tractions exerted by cells within three-dimensional matrices. Nat Methods 7, 969–971.
Liu Z, Ho CH, Grinnell F (2014). The different roles of myosin IIA and myosin IIB in contraction of 3D collagen matrices by human fibroblasts. Exp Cell Res 326, 295–306.
Liu Z, Tan JL, Cohen DM, Yang MT, Sniadecki NJ, Ruiz SA, Nelson CM, Chen CS (2010). Mechanical tugging force regulates the size of cell–cell junctions. Proc Natl Acad Sci USA 107, 9944–9949.
Lo CM, Buxton DB, Chua GCH, Dembo M, Adelstein RS, Wang YL (2004). Nonmuscle myosin IIB is involved in the guidance of fibroblast migration. Mol Biol Cell 15, 982–989.
Lyle KS, Corleto JA, Wittmann T (2012). Microtubule dynamics regulation contributes to endothelial morphogenesis. Bioarchitecture 2, 220–227.
Mehta D, Malik AB (2006). Signaling mechanisms regulating endothelial permeability. Physiol Rev 86, 279–367.
Münster S, Jawerth LM, Broedersz C, Weitz DA, Fabry B (2010). Non-linear mechanical properties of collagen networks during cyclic loading. Biophys J 98, 558A–559A.
Ng MR, Besser A, Danuser G, Brugge JS (2012). Substrate stiffness regulates cadherin-dependent collective migration through myosin-II contractility. J Cell Biol 199, 545–563.
Nguyen DHT, Stapleton SC, Yang MT, Cha SS, Choi CK, Galie PA, Chen CS (2013). Biomimetic model to reconstitute angiogenic sprouting morphogenesis in vitro. Proc Natl Acad Sci USA 110, 6712–6717.
Oubaha M, Lin MI, Margaron Y, Filion D, Price EN, Zon LI, Côté JF, Gratton JP (2012). Formation of a PKCζ/β-catenin complex in endothelial cells promotes angiopoietin-1–induced collective directional migration and angiogenic sprouting. Blood 120, 3371–3381.
Petrie RJ, Gavara N, Chadwick RS, Yamada KM (2012). Nonpolarized signaling reveals two distinct modes of 3D cell migration. J Cell Biol 197, 439–455.
Rafii S, Bulter JM, Ding BS (2016). Angiocrine functions of organ-specific endothelial cells. Nature 529, 316–325.
Rao RR, Peterson AW, Ceccarelli J, Putnam AJ, Stegemann JP (2012). Matrix composition regulates three-dimensional network formation by endothelial cells and mesenchymal stem cells in collagen/fibrin materials. Angiogenesis 15, 253–264.
Rausch S, Das T, Soiné JR, Hofmann TW, Boehm CH, Schwarz US, Boehm H, Spatz JP (2013). Polarizing cytoskeletal tension to induce leader cell formation during collective cell migration. Biointerphases 8, 32.
Ribatti D, Nico B, Crivellato E (2011). The role of pericytes in angiogenesis. Int J Dev Biol 55, 261–268.
Scarpa E, Mayor R (2016). Collective cell migration in development. J Cell Biol 212, 143–155.
Shewan AM, Maddugoda M, Kraemer A, Stehbens SJ, Verma S, Kovacs EM, Yap AS (2005). Myosin 2 is a key rho kinase target necessary for the local concentration of E-cadherin at cell–cell contacts. Mol Biol Cell 16, 4531–4542.
Shih W, Yamada S (2010). Myosin IIA dependent retrograde flow drives 3D cell migration. Biophys J 98, L29–L31.
Shin Y, Jeon JS, Han S, Jung GS, Shin S, Lee SH, Sudo R, Kamm RD, Chung S (2011). In vitro 3D collective sprouting angiogenesis under orchestrated ANG-1 and VEGF gradients. Lab Chip 11, 2175–2181.
Smutny M, Cox HL, Leerberg JM, Kovacs EM, Conti MA, Ferguson C, Hamilton NA, Parton RG, Adelstein RS, Yap AS (2010). Myosin II

isoforms identify distinct functional modules that support integrity of the epithelial zonula adherens. Nat Cell Biol 12, 696–702.
Thievessen I, Fakhri N, Steinwachs J, Kraus V, McIsaac RS, Gao L, Chen BC, Baird MA, Davidson MW, Betzig E, *et al*. (2015). Vinculin is required for cell polarization, migration, and extracellular matrix remodeling in 3D collagen. FASEB J 29, 4555–4567.
Trappmann B, Baker BM, Polacheck WJ, Choi CK, Burdick JA, Chen CS (2017) Matrix degradability controls multicellularity of 3D cell migration. Nat Commun 8, 371.
Tseng Q, Duchemin-Pelletier E, Deshiere A, Balland M, Guillou H, Filhol O, Théry M (2012) Spatial organization of the extracellular matrix regulates cell–cell junction positioning. Proc Natl Acad Sci USA 109, 1506–1511.
Valent ET, van Nieuw Amerongen GP, van Hinsbergh VW, Hordijk PL (2016). Traction force dynamics predict gap formation in activated endothelium. Exp Cell Res 347, 161–170.
Wimmer R, Cseh B, Maier B, Scherrer K, Baccarini M (2012). Angiogenic sprouting requires the fine tuning of endothelial cell cohesion by the Raf-1/Rok-α complex. Dev Cell 22, 158–171.
Yang MT, Reich DH, Chen CS (2011). Measurement and analysis of traction force dynamics in response to vasoactive agonists. Integr Biol 3, 663–674.
Yeh YT, Serrano R, Francois J, Chiu JJ, Li YJ, Del Alamo JC, Chien S, Lasheras JC (2018). Three-dimensional forces exerted by leukocytes and vascular endothelial cells dynamically facilitate diapedesis. Proc Natl Acad Sci USA 115, 133–138.